IVYSPRING INTERNATIONAL PUBLISHER

Theranostics

2019; 9(14): 4192-4207. doi: 10.7150/thno.34157

Research Paper

PMMA-Fe_3O_4 for internal mechanical support and magnetic thermal ablation of bone tumors

Kexiao Yu[1,2#], Bing Liang[2#], Yuanyi Zheng[3]✉, Agata Exner[4], Michael Kolios[5], Tiantian Xu[6], Dajing Guo[7], Xiaojun Cai[3], Zhigang Wang[2], Haitao Ran[2], Lei Chu[1]✉ and Zhongliang Deng[1]✉

1. Department of Orthopaedics, Second Affiliated Hospital of Chongqing Medical University, 76 Linjiang Road, Yuzhong Distinct, Chongqing, 400010, P. R. China.
2. Chongqing Key Laboratory of Ultrasound Molecular Imaging, Second Affiliated Hospital of Chongqing Medical University, 76 Linjiang Road, Yuzhong Distinct, Chongqing, 400010, P. R. China.
3. Shanghai Institute of Ultrasound in Medicine, Shanghai Jiao Tong University Affiliated Sixth People's Hospital, 600 Yishan Road, Xuhui Distinct, Shanghai, 200233, P. R. China.
4. Radiology department of University Hospital, Case Western Reserve University, 10900 Euclid Ave, Cleveland, OH, 44106, USA.
5. Department of Physics, Ryerson University, Toronto, 350 Victoria Street Toronto, Ontario M5B 2K3, Ontario, Canada
6. Guangdong Provincial Key Laboratory of Robotics and Intelligent System, Shenzhen Institutes of Advanced Technology, Chinese Academy of Sciences, Shenzhen 518055, China
7. Department of Radiology, Second Affiliated Hospital of Chongqing Medical University, 76 Linjiang Road, Yuzhong Distinct, Chongqing, 400010, P. R. China.

# Kexiao Yu and Bing Liang are co-first authors who contributed equally to this study.

✉ Corresponding authors: Prof.Yuanyi Zheng, Shanghai Institute of Ultrasound in Medicine, Shanghai Jiao Tong University Affiliated Sixth People's Hospital, 600 Yishan Road, Xuhui Distinct, Shanghai, 200233, P. R. China. E-mail: zhengyuanyi@163.com; Dr. Lei Chu, Second Affiliated Hospital of Chongqing Medical University, 76 Linjiang Road, Yuzhong Distinct, Chongqing, 400010, P. R. China. E-mail: Chulei2380@163.com; Prof. Zhongliang Deng, Second Affiliated Hospital of Chongqing Medical University, 76 Linjiang Road, Yuzhong Distinct, Chongqing, 400010, P. R. China. E-mail: zhongliang.deng@yahoo.com.

Received: 2019.02.16; Accepted: 2019.05.09; Published: 2019.05.31

Abstract

Background: Minimally invasive modalities are of great interest in the field of treating bone tumors. However, providing reliable mechanical support and fast killing of tumor cells to achieve rapid recovery of physical function is still challenging in clinical works.

Methods: A material with two functions, mechanical support and magnetic thermal ablation, was developed from Fe_3O_4 nanoparticles (NPs) distributed in a polymethylmethacrylate (PMMA) bone cement. The mechanical properties and efficiency of magnetic field-induced thermal ablation were systematically and successfully evaluated *in vitro* and *ex vivo*. CT images and pathological examination were successfully applied to evaluate therapeutic efficacy with a rabbit bone tumor model. Biosafety evaluation was performed with a rabbit *in vivo*, and a cytotoxicity test was performed *in vitro*.

Results: An NP content of 6% Fe_3O_4 (PMMA-6% Fe_3O_4, m_{Fe}: 0.01 g) gave the most suitable performance for *in vivo* study. At the 56-day follow-up after treatment, bone tumors were ablated without obvious side effects. The pathological examination and new bone formation in CT images clearly illustrate that the bone tumors were completely eliminated. Correspondingly, after treatment, the tendency of bone tumors toward metastasis significantly decreased. Moreover, with well-designed mechanical properties, PMMA-6%Fe_3O_4 implantation endowed tumor-bearing rabbit legs with excellent bio-mimic bone structure and internal support. Biosafety evaluation did not induce an increase or decrease in the immune response, and major functional parameters were all at normal levels.

Conclusion: We have presented a novel, highly efficient and minimally invasive approach for complete bone tumor regression and bone defect repair by magnetic thermal ablation based on PMMA containing Fe_3O_4 NPs; this approach shows excellent heating ability for rabbit VX2 tibial plateau tumor ablation upon exposure to an alternating magnetic field (AMF) and provides mechanical support for bone repair. The new and powerful dual-function implant is a promising minimally invasive agent for the treatment of bone tumors and has good clinical translation potential.

Key words: magnetic thermal ablation; PMMA; bone tumors; mechanical support, fast clinical translation

Introduction

The mortality of bone tumors is exceptionally high, and the prognosis is poor, seriously threatening patient lives [1-3]. A devastating consequence of bone tumors is bone destruction, which causes disastrous skeletal-related events. These intractable clinical problems, such as unbearable bone pain, pathological fractures, spinal cord compression, bone deformity and hypercalcemia, are great challenges to surgeons [4, 5]. With the loss of bone support, patients are not able to stand and could become bedridden for an extended time. These complications significantly reduce quality of life and increase mortality [6]. Surgical resection is the traditional choice for primary bone cancer; however, the extensive trauma imposed by major surgery and often amputation is a serious physical and spiritual pain for patients. Therefore, minimally invasive strategies for treating bone tumors are urgently needed. Recently developed percutaneous vertebroplasty (PVP) and percutaneous kyphoplasty (PKP), which are minimally invasive clinical surgeries, could efficiently solve this critical issue. These minimally invasive techniques have been used to treat pathological fractures and decrease pain. Unfortunately, these strategies aim to increase the survival time and quality of life and are unable to effectively decrease the bone tumor burden [5, 7, 8]. Radiotherapy and chemotherapy are commonly used to treat bone tumors, but the bone microenvironment provides a protective alcove for tumor cells to resist clinical radiotherapy and chemotherapy, reducing the curative effect [9-11].

Hyperthermia, which can be applied with the aim of increasing the temperature of tumor tissues to directly destroy tumor cells, provides another promising treatment modality for patients [12, 13]. Additionally, hyperthermia is one of the clinically applied therapeutic modalities for solid tumor regression when combined with radiotherapy or chemotherapy, as demonstrated by several randomized studies [14-17], including studies of hyperthermia induced by radiofrequency, microwave and high-intensity focused ultrasound [18, 19]. Light-induced hyperthermia based on functional nanoparticles (NPs), such as Au, MoS_2 and graphene, is another new hyperthermia modality. When a metal NP is illuminated, part of the intercepted light gets absorbed and ultimately dissipated into heat. This photothermal therapy can also induce tumor cell death, but the limited penetration depth of light severely restricts the application of photothermal therapy to bone tumors [20, 21]. Magnetic thermal ablation, which involves magnetic nanoparticles, such as Fe_3O_4 and γ-Fe_2O_3, via the application of a controllable external alternating magnetic field (AMF), provides a promising alternative strategy to achieve tumor ablation [12, 13, 22]. In addition to the excellent high heating efficiency, the greatest advantage is the lack of biological barriers, allowing the application of magnetic thermal ablation to both superficial and deeply seated tumors. This capability is based on the specific physical features of the adopted radiofrequency electromagnetic waves [13, 23]. Moreover, magnetic NPs can perform different functions when mixed with specific media. This multifunction potential increases the possibilities for developing a novel hyperthermic strategy for treating bone tumors.

Among the greatest limitations of all strategies for treating bone tumors are the inability to quickly repair the bone defect, provide reliable mechanical support to achieve fast physical function recovery and avoid potential damage to some important organs, such as the spinal cord, even if the above methods can induce complete tumor cell death. To address these challenges, we have developed a dual-function injectable material inspired by the bone cement that is widely used for the clinical treatment of spinal compression fractures [24, 25]. This formulation is aimed at inducing tumor cell death while quickly filling the bone defect simultaneously to provide internal support for the body weight in a minimally invasive manner by injection. Polymethyl-methacrylate (PMMA) bone cement, as an FDA-approved material, has been used as a grouting agent in total joint replacement surgery for more than 50 years [26] and is also widely used in PVP for the treatment of osteoporotic fractures [24, 27] because of its excellent characteristics, including its stable solidifying process, mechanical strength and good biocompatibility. However, for bone tumor clinical applications, PMMA bone cement can be used only for mechanical support implantation and cannot kill tumor cells or prevent tumor progression. In additional, PMMA is of limited use in patients suffering from osteoporosis owing to its excessively strong stiffness [28]. Moreover, the short window for operation and polymerization heat restrict the utilization and promotion of PMMA in clinical bone tumor treatment [29]. Fe_3O_4 NPs have been widely used in MH or as a magnetic resonance imaging contrast agent with good biocompatibility [30]. The combination of PMMA bone cement and Fe_3O_4 NPs and investigation the properties of this mixture have gradually attracted interest among researchers. A report described PMMA bone cement containing Fe_3O_4 for thermal ablation treatment of cancer *in vitro*, but this study did not demonstrate the approach *in vivo*, especially not its mechanical properties and in situ mimic efficiency with clinical bone tumors [31].

Some researchers have presented a magnetic thermal ablation approach by distributing Fe_3O_4 NPs inside calcium phosphate cement (CPC) [32]. Though the treatment effect *in vivo* was excellent, the drawbacks include poor injectability, long setting time and the need to improve the degradability of CPC [33]. PMMA bone cement provides good injectability for local injection, a shorter setting time to fix Fe_3O_4 NPs to prevent leakage during the liquid-solid phase transition, faster repair of bone defects to achieve fast recovery, and further non-degradability to ensure that there is no Fe_3O_4 NP leakage over a patient's long lifetime.

Herein, we designed an injectable and highly efficient magnetic material by distributing Fe_3O_4 NPs inside PMMA bone cement for the minimally invasive magnetic ablation of bone tumors and to achieve internal mechanical support. PMMA-Fe_3O_4 in the liquid phase was accurately injected into the bone tumor to fill the bone defect under computed tomography (CT) guidance. After PMMA-Fe_3O_4 transformed to the solid phase, an AMF was applied externally. The thermal ablation that occurred in the vicinity of the magnetic bone cement induced tumor cell coagulative necrosis, and the solid cement simultaneously provided an ideal mechanical support for fast physical function recovery to help relieve pain in the patient as soon as possible. Interestingly, we found that the addition of Fe_3O_4 to PMMA significantly improved the quality of the PMMA bone cement, decreasing the potential for fractures in adjacent bone after intervention, while simultaneously demonstrating good biosafety and biocompatibility. Then, for the first time, we employed the established in situ tibial plateau bone tumor model in New Zealand rabbits via a coaxial puncture needle, which simulated the clinical characteristics of bone tumors to the greatest extent, to evaluate the therapeutic effect and prognosis of PMMA-Fe_3O_4. Most importantly, the combined thermal ablation and mechanical support functions are based on materials that are generally regarded as safe and already clinically utilized. All of the above-mentioned benefits could facilitate further rapid clinical translation and provide an instructive way for surgeons to implement bone tumor treatment.

Results and Discussion

Design and synthesis of PMMA-Fe_3O_4 bone cement

In this work, we successfully prepared magnetic PMMA bone cement **(Figure 1A-D)** for magnetic thermal ablation to ablate tumors. As shown in **Table 1**, cements with 0, 3, 6 and 9% Fe_3O_4 were designed to test the heating efficacy and mechanical properties with different iron contents.

Table 1. Composition of PMMA-Fe_3O_4.

Bone Cement	Powder (g)		MMA monomer (mL)
	Fe_3O_4	PMMA	
PMMA	0	2.6	1
PMMA-3%Fe_3O_4	0.1095	2.6	1
PMMA-6%Fe_3O_4	0.2260	2.6	1
PMMA-9%Fe_3O_4	0.3560	2.6	1

Morphology characterization of PMMA-Fe_3O_4 bone cement

SEM images of Fe_3O_4 NPs and PMMA-Fe_3O_4 powders are shown in **Figure S1A-D**; the size of Fe_3O_4 NP was 120.60 ± 38.95 nm, and the size of PMMA was 30 ± 12.36 μm. It was reported that the transition from a polydomain to a monodomain state of Fe_3O_4 NPs is around 60 nm [34], and the mean size of the applied Fe_3O_4 NPs was 120.60 ± 38.95 nm (**Figure S1C**). Therefore, the Fe_3O_4 NPs in this study were above the monodomain limit. After mixing, the Fe_3O_4 NPs were uniformly distributed in the PMMA powder, and there was no congregated crystallization or connection between the NPs. SEM images of the PMMA bone cement showed a cobblestone-like material, which is the solid phase of PMMA, that was densely distributed, and the zirconium dioxide particles were closely surrounded by PMMA **(Figure 1E-F)**. Due to the special radiographic functionality of PMMA bone cement, zirconium dioxide particles were added as radiopaque agents to enable CT-guided injection and to obtain precise and objective CT image information. SEM images of the mixture with 6% Fe_3O_4 NPs **(Figure 1G-H)** show many dense and small dots uniformly and densely distributed in the PMMA matrix, which is white and bright, indicating that Fe_3O_4 NPs successfully integrated into the PMMA matrix without damaging its original structure. It was demonstrated that, given the strength of this stable internal structure, Fe_3O_4 NPs rarely escaped from the tumor tissue or penetrated solidified material, thus preventing Fe_3O_4 NPs from accumulating in sensitive organs and improving the biosafety of PMMA-6%Fe_3O_4 magnetic materials. The results of energy spectrum **(Figure 1J)** showed the atomic percentage of C, O, Fe and Zr were 48.19%, 39.02%, 5.55% and 7.24%, respectively. The weight percentage of C, O, Fe and Zr were 26.63%, 28.73%, 14.25% and 30.39%, respectively. The element mappings **(Figure 1K-N)** exhibited a uniform distribution of ferrous elements with carbonaceous and oxygen frameworks, indicating good dispersity of Fe_3O_4 NPs in both the liquid and solid phases. More importantly, a uniform distribution of magnetic NPs

means a uniform temperature increase, which guarantees safety during heating. The hysteresis loops **(Figure 1I and Figure S1E)** of PMMA-6%Fe_3O_4 and Fe_3O_4 NPs were narrow, showing their soft magnetic performance. Under 300 K (26.85 °C), the saturation magnetization values of PMMA-6%Fe_3O_4 and Fe_3O_4 NPs were 8.62 emu/g and 93.99 emu/g, respectively, and the coercive forces of PMMA-6%Fe_3O_4 and Fe_3O_4 NPs were 84.45 Oe and 103.34 Oe, respectively. For these soft magnetic materials, the relatively low coercive force and hysteresis loss properties further demonstrated that PMMA-6%Fe_3O_4 could be heated by AMF due to the hysteresis loss of the material and eddy current losses [35].

Evaluation of injectability of PMMA-Fe_3O_4 bone cement

The injectability of PMMA-Fe_3O_4 is one of the most basic and significant factors in its application. This parameter was initially evaluated to demonstrate that in situ injection of the PMMA-Fe_3O_4 could be performed in a minimally invasive manner. Generally, 70 N is the maximum force that can reasonably be applied to a syringe by healthy human thumbs [36]. As shown in **Figure 2D**, the injectability of PMMA-Fe_3O_4 was more than 90% and increased with increasing Fe_3O_4 NP content, indicating excellent injectability. Even when injected into water, the magnetic bone cement maintained its shape and polymerized into a solid implant **(Figure S2A-D)**. The benign injectability and applicability of PMMA-Fe_3O_4 demonstrated that this type of minimally invasive injectable implant can remain integrated after injection into bone tissues with a full blood supply via CT guidance.

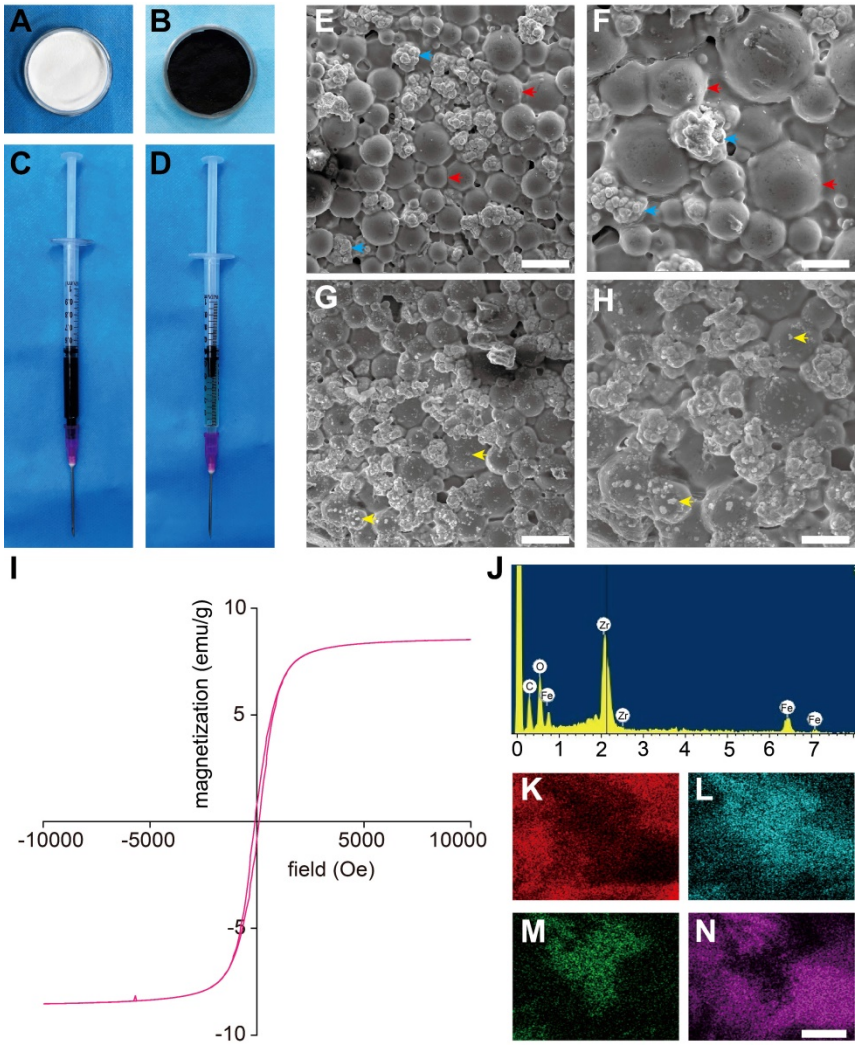

Figure 1. Characterization of PMMA-Fe_3O_4 magnetic compressive materials. (A-D) Morphological photos of PMMA-6%Fe_3O_4: (A) PMMA powder, (B) Fe_3O_4 nanoparticles, (C) MMA monomer, (D) injectable PMMA-6%Fe_3O_4. (E) Low-magnification SEM image of polymerized PMMA. The scale bar is 50 μm. (F) High-magnification SEM image of polymerized PMMA. The scale bar is 20 μm. (G) Low-magnification SEM image of polymerized PMMA-6%Fe_3O_4. The scale bar is 50 μm. (H) High-magnification SEM image of polymerized PMMA-6%Fe_3O_4. The scale bar is 20 μm (red arrow: poly methyl methacrylate, blue arrow: zirconium dioxide particulate, yellow arrow: Fe_3O_4 nanoparticles). (I) Magnetic hystersis loop of polymerized PMMA-6%Fe_3O_4. (J) Energy spectrum of PMMA-6%Fe_3O_4. (K-N) Element mapping of the surface of polymerized PMMA-6%Fe_3O_4 solid implant (K: C, L: O, M: Fe, N: Zr, the scale bar is 2.5 μm).

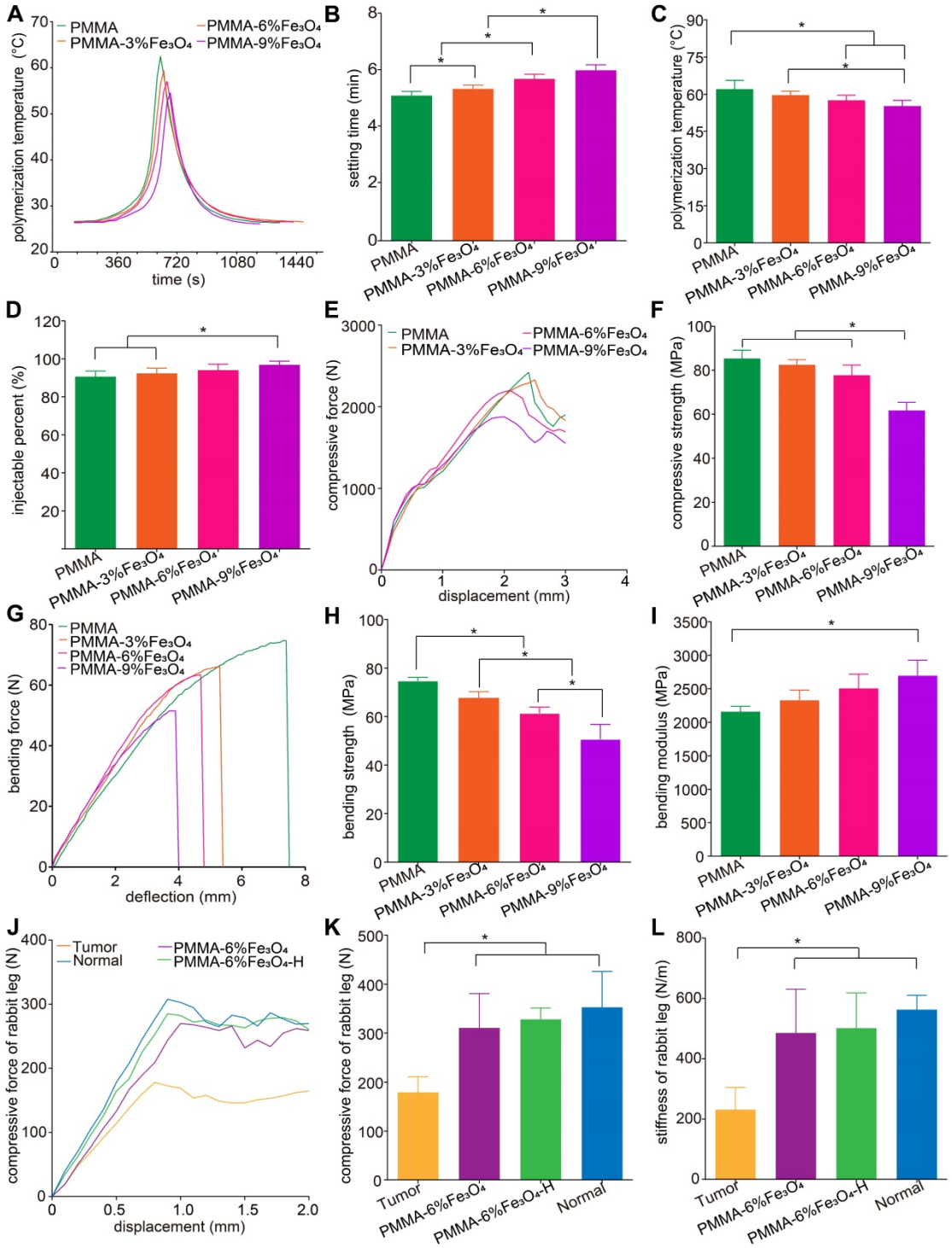

Figure 2. Physical properties of PMMA-Fe_3O_4 magnetic compressive materials. (A) Polymerization temperature-time curves of PMMA with different Fe_3O_4 nanoparticle contents. (B) Setting time of PMMA with different Fe_3O_4 nanoparticle contents. (C) Polymerization temperature of PMMA with different Fe_3O_4 nanoparticle contents. (D)The injectability of PMMA with different Fe_3O_4 nanoparticle contents. (E) The load-displacement curve and (F) corresponding compressive strength of PMMA with different Fe_3O_4 nanoparticle contents. (G) The load-deflection curve of the three-point bending test, (H) corresponding bending strength and (I) bending modulus of PMMA with different Fe_3O_4 nanoparticle contents. (J) The load-displacement curves of tibial plateau tumor (Tumor), healthy rabbit tibia (Normal), tumor-planted rabbit tibia with implantation of PMMA-6%Fe_3O_4 and tumor-planted rabbit tibia with PMMA-6%Fe_3O_4 under magnetic thermal ablation (PMMA-6%Fe_3O_4-H). (K) Corresponding compressive force and (L) stiffness.

Exotherm during the polymerization of PMMA-Fe_3O_4 bone cement

The setting time reflects the polymerization time, which is important for achieving fast repair of bone defects. It is known that patients with pain caused by a vertebral compression fracture can receive immediate pain relief and fast restoration of physical function as long as the bone cement is polymerized, which generally takes less than twenty minutes.

As shown in **Figure 2A-B**, the setting time ranged from 5 to 6 min among the bone cements with the various iron contents. Statistical analysis showed that setting time significantly increased with increasing iron content. Nonetheless, the solidification process was rapid in all groups, which indicates that the setting time of this clinically applied bone cement is minimally disrupted by the addition of small amounts of Fe_3O_4. A slight increase in setting time indicates more time in the liquid phase, which is beneficial for effective injection under CT guidance.

As shown in **Figure 2A-C**, the highest temperatures in the center of the material were 62.1 ± 3.5 °C, 59.7 ± 1.5 °C, 57.6 ± 2.0 °C and 55.2 ± 2.4 °C for PMMA, PMMA-3%Fe_3O_4, PMMA-6%Fe_3O_4, and PMMA-9%Fe_3O_4, respectively. Although the highest polymerization temperature in the center decreased with increasing iron content, this temperature was still greater than 50 °C. Therefore, the influence of a high spontaneous polymerization temperature on tumor cells/tissue needs to be further explored. As a consequence, we used PMMA-6%Fe_3O_4 without heat as a control group for an *in vivo* study.

Mechanical properties of PMMA-Fe_3O_4 bone cement

As a fast bone repair material, PMMA-Fe_3O_4 has the advantage of a rapid liquid-solid phase transition, providing anticompression and antishear capabilities, which are dominant factors for supporting body weight. Therefore, the International Organization for Standardization published its ISO5833:2002(E) guideline with standardized specifications for the mechanical properties in each clinically applied bone cement; in detail, this guideline indicates that the compressive strength, bending strength and bending modulus must be higher than 70 MPa, 50 MPa and 1800 MPa, respectively. The mechanical properties of the different bone cements changed with the iron content and were less than the specified values in the ISO5833:2002(E) guidelines, indicating that the bone cements were not sufficiently strong to support body weight and cannot be used for *in vivo* applications. This evaluation is one of the most important steps in selecting a safe and reliable magnetic bone cement to guarantee fast clinical translation to benefit bone tumor patients.

The load-displacement curves from the compression test and load-deflection curve from the three-point bending test in this study are shown in **Figure 2E and Figure 2G**. From the curves, the compressive strength **(Figure 2F)**, bending strength **(Figure 2H)** and bending modulus **(Figure 2I)** were calculated. Ultimately, PMMA-9%Fe_3O_4 was excluded from subsequent experiments because the compressive strength was lower than 70 MPa. Excessive mechanical strength may increase the risk of adjacent vertebral fracture after PVP and PKP [37-39]. Therefore, many researchers tried to add various media, such as hyaluronic acid [40], linoleic acid [41], saline solution [28] and even patients' blood [42], to decrease the mechanical strength to make PMMA bone cements more suitable for cancellous bone, especially osteoporotic bone. In summary, as long as the mechanical strength meets the ISO5833:2002(E) guideline, appropriate strength reduction is a safe procedure and is even preferred for clinical applications.

In addition to measuring the mechanical properties of the PMMA-Fe_3O_4 material itself, it is also important to check whether this material can precisely restore the anti-compression capability of a tumor-implanted leg. Additionally, we were curious whether the mechanical properties would differ between the heated and unheated groups after the material was injected into the tumor. The load-displacement curves of the *ex vivo* tibial plateau compression test are shown in **Figure 2J**. The compressive forces were 179.0 ± 32.0 N, 310.3 ± 70.5 N, 328.0 ± 23.5 N, and 353.0 ± 73.1 N for the Tumor, PMMA-6%Fe_3O_4, PMMA-6%Fe_3O_4-H and Normal groups, respectively **(Figure 2K)**. The stiffnesses were 231.7 ± 73.4 N/mm, 485.7 ± 145.1 N/mm, 501.3 ± 117.0 N/mm, and 562.7 ± 83.0 N/mm for the Tumor, PMMA-6%Fe_3O_4, PMMA-6%Fe_3O_4-H and Normal groups, respectively **(Figure 2L)**. This result indicates that tumor growth in the tibial plateau significantly worsened the mechanical properties of the bone, making the bone susceptible to compression deformation and fracture. After injection of PMMA-6%Fe_3O_4 and its transformation to a solid, regardless of whether heating was used, the mechanical properties recovered and showed no statistically significant difference from the normal tibial plateau in *ex vivo* measurements.

In vitro magnetic-thermal-induced thermal efficiency evaluation

It is known that magnetic materials can convert electromagnetic energy into heat because of Brown and Néel relaxation, hysteresis loss or eddy current loss [43, 44]. The SAR value for Fe in PMMA-6%Fe_3O_4 was 389 W/g under this AMF. As illustrated in the images in **Figure 3A**, the color of the saline solution without iron barely changed. As the iron content increased and time passed, the temperature of the saline solution increased remarkably **(Figure 3B)**. The temperature reached 63.6 ± 2.3 °C, 76.3 ± 3.0 °C and 82.9 ± 2.6 °C for 150 μL of PMMA-6%Fe_3O_4 (m_{Fe}: 0.01 g) at the time points of 60 s, 120 s and 180 s,

respectively ($p < 0.05$). The temperature reached only 34.8 ± 0.6 °C and 60.1 ± 2.2 °C for 150 μL of PMMA and PMMA-3%Fe_3O_4, respectively, after 180 s of heating. For 100 μL, 150 μL and 200 μL of PMMA-6%Fe_3O_4, the temperature increased to 63.6 ± 2.3 °C, 70.1 ± 1.4 °C and 80.5 ± 4.3 °C, respectively, after 60 s of heating ($p < 0.05$) **(Figure 3C)**. As the load of Fe_3O_4 powder in the bone cement increased, the temperature increased linearly with the AMF, proving significant magnetic field-mediated thermal conversion of the PMMA-Fe_3O_4 bone cement. The results of this experiment precluded the use of PMMA-3%Fe_3O_4 because of its low heating efficiency.

In the aforementioned work, the PMMA-9%Fe_3O_4 bone cement was excluded because of its poor mechanical properties (compressive strength was less than 70 MPa), which did not meet the ISO5833:2002(E) guideline. Additionally, compared with PMMA-6%Fe_3O_4 and PMMA-9%Fe_3O_4, the heating efficiency of PMMA-3%Fe_3O_4 cement was lowest, and it was not able to achieve the target temperature for tumor ablation and action duration. PMMA-6%Fe_3O_4 bone cement, with good magnetic thermal performance and appropriate mechanical properties, was the most suitable for *in vivo* study.

Evaluation of magnetic-thermal-induced temperature distribution and ablation efficiency *ex vivo*

During magnetic thermal treatment, it is a challenge to limit the therapy area in the tumor and avoid injury to surrounding healthy tissue. Infrared imaging can measure surface temperatures but has failed to monitor temperatures in deep tissue. Although MRI can monitor temperatures in deep areas, a locally high content of magnetic material, such as Fe_3O_4 NPs, will produce defects upon MRI examination, which causes real-time MRI monitoring to fail. Tay ZW, et al. shaped magnetic fields to "gate" the heating only to selected regions under MRI guidance [45]. Jessica F. Liu, et al. developed a magnetic device containing a sharp zero point, allowing for magnetically driven spatially targeted drug release from thermally sensitive liposomal drug carriers [46]. Therefore, it is highly necessary to take actions such as performing experiments to evaluate heating and ablation areas. We placed the bone

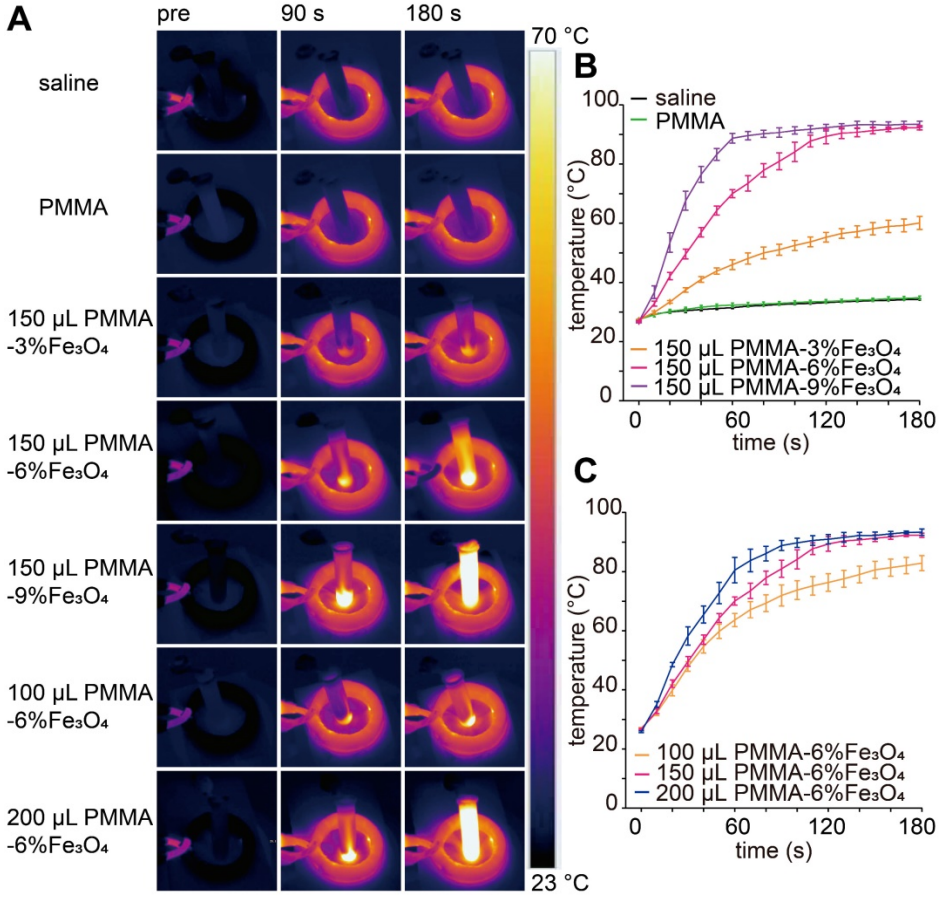

Figure 3. Therapeutic performance of the PMMA-Fe_3O_4 magnetic compressive materials for magnetic thermal ablation. (A) *In vitro* thermal images of PMMA with different volumes and Fe_3O_4 nanoparticle contents for varied durations; PMMA without Fe_3O_4 and saline solution were used to treat the control groups. (B) The corresponding temperature-time curve at different masses of Fe_3O_4 and (C) PMMA-6%Fe_3O_4 with different volumes.

cement in excised bovine liver and heated it to simulate heating bone tumors *in vivo*. The goal of this experiment was to clarify the relationship between heating time and ablation area and further control the ablation area to cover all tumors and prevent extensive injury of the surrounding healthy tissues.

As shown in **Figure S4A**, thermal images of a 2 cm × 2 cm × 4 cm section of excised bovine liver containing hemispheric PMMA-6%Fe_3O_4 (75 μL, m_{Fe}: 0.005 g) were obtained to simulate the evaluation of the change in heating temperature in deep tissue; the temperature increased rapidly in the closed tissue and decreased obviously with increasing distance **(Figure S4C)**. The temperature decreased from 82.7 ± 13.8 °C (1 mm away from the surface of the embedded PMMA-6%Fe_3O_4) to 71.2 ± 5.5 °C, 61.4 ± 2.8 °C, 53.8 ± 0.4 °C, 47.5 ± 0.2 °C, 44.5 ± 0.3 °C, 40.8 ± 0.2 °C, 38.4 ± 0.5 °C, and 36.9 ± 0.9 °C (1.5, 2, 2.5, 3, 3.5, 4, 4.5, and 5 mm, respectively, away from the surface of the embedded PMMA-6%Fe_3O_4) after 150 s of heating **(Figure S4C)**. This result indicates that high temperatures can be used to cover all areas of PMMA-6%Fe_3O_4 bone cement while avoiding high temperature disruptions of large areas of the surrounding healthy tissue.

Although the area subjected to high temperature can be controlled, the real ablation distance must be checked. As **Figure S4B** shows, the thermal images acquired from the surface of the excised bovine liver embedded with 150 μL of PMMA-6%Fe_3O_4 (m_{Fe}: 0.01 g) showed that the temperature increased with time, and the surface temperature reached only 40 ± 1.3 °C after heating for 180 s, which makes it easy to conclude that the surface temperature does not reflect the deep temperature **(Figure S4D)**. Segmenting the heated liver in half and removing the bone cement showed that the ablated liver tissue became white, and the ablation distance could be measured easily **(Figure S4F)**. The corresponding visually measured ablation distance is shown in **Figure S4E**. The ablated tissue distances were 1.38 ± 0.12 mm, 3.06 ± 0.24 mm, and 4.82 ± 0.23 mm for 120 s, 150 s and 180 s, respectively. The pathological examination of hematoxylin-eosin (H&E)-stained heated excised bovine liver further demonstrated that the ablation efficiency was exact and controllable. Prussian blue staining demonstrated a lack of Fe_3O_4 particulate leakage during heating, further illustrating that this magnetic bone cement is stable during heating **(Figure S4G)**.

It has been reported that irreversible cellular damage occurs when heating tissues at 43 °C for several hours, and cell death arises with continuous heat for 4-6 min at 50-55 °C. When the temperature reaches 60-100 °C, tissue coagulation occurs nearly immediately, while at temperatures greater than 100 °C, tissue becomes vaporized and carbonized [47-50]. Our results are consistent with the literature, and our target temperature is greater than 60 °C, which can effectively and quickly induce tumor necrosis and stimulate the immune system through the expression of heat shock proteins (HSPs). In summary, according to the above two experiments, the distance that was heated to temperatures greater than 60 °C was limited to 2 mm, the distance heated to temperatures greater than 47 °C was limited to 3 mm, and the ablation distance was limited to 3 mm, preventing damage to normal tissues while enabling ablation of tumors.

Biosafety of PMMA-6%Fe_3O_4 *in vivo* and *in vitro*

PMMA bone cement is a widely used material for bone filling and repair in orthopedics that exhibits excellent biocompatibility and biosafety [26], Additionally, Fe_3O_4 is used as a contrast agent in MRI. Therefore, the mixed material should exhibit comparable biocompatibility and safety. Based on the cell apoptosis results measured by flow cytometry **(Figure S5)**, the proportion of living cells was 94.02 ± 0.80% in the control group and 92.04 ± 0.74% in the experimental group. There was no statistically significant difference between the two groups (p > 0.05). The cell experiment indicated that PMMA-6%Fe_3O_4 had no obvious toxic effects. As shown in **Figure 4A**, there were no inflammatory cells and no obvious damage in the muscle tissues around the PMMA-6%Fe_3O_4, which suggests good biocompatibility. Compared to the corresponding tissues in the normal rabbit, the heart, liver, spleen, lung and kidney tissue showed no changes, and no black Fe_3O_4 particles were found in these viscera, which indicates a lack of organic injury after implantation of this bone cement and an inability of Fe_3O_4 NPs to escape from the bone cement **(Figure S6)**. The serum tests for heart function, liver function and kidney function, including ALT, AST, CR, BUN, CK and LDH assessments, revealed no significant difference at each test point **(Figure 4B)**. The blood tests included WBC, RBC, HB and PLT counts, which were in the normal range **(Table S1)**. These results indicate no effects on heart function, liver function, kidney function and blood function, illustrating the good biosafety of locally injected PMMA-6%Fe_3O_4 *in vivo*. These results clearly demonstrate the excellent biocompatibility and biosafety of magnetic bone cement.

With the application of inductively coupled plasma optical emission spectrometer (ICP-OES) quantitative measurement, the iron concentrations of PMMA-6%Fe_3O_4 in the first batch with and without heating were 59.85 ± 0.29 mg/g and 60.18 ± 0.40

mg/g, respectively, indicating no significant difference between the two groups ($p > 0.05$). Furthermore, the Prussian blue staining results for the organs were negative, illustrating that no Fe_3O_4 NPs escaped from the PMMA bone cement after heating **(Figure S7)**. The iron concentrations of PMMA-6%Fe_3O_4 in the second batch with and without attraction by the $Nd_2Fe_{14}B$ magnet were 59.90 ± 0.20 mg/g and 60.03 ± 0.18 mg/g, respectively, showing no significant difference between the two treatments. These results strongly illustrated that no Fe_3O_4 NPs escaped after magnetic heating *in vivo* and even exposure in a strong magnetic field.

Preparation of a tumor model in the rabbit tibial plateau with a VX2 tumor mass

Generally, nude mouse models with flank xenograft tumors are widely used for magnetic thermal ablation experiments [35, 51, 52], but these models cannot simulate the real change in bone, which may decrease the reliability of therapeutic effects and interfere with fast clinical translation. The basic signs and characteristics of a bone tumor include destruction of bone, formation of tumorous bone, reaction of the periosteum, tumefaction of soft tissue and a change in neighboring tissue [53]. Therefore, it is important to establish an ideal bone tumor model to simulate bone tumor invasion and verify the efficacy of magnetic thermal ablation. The rabbit tibial plateau tumor model is an alternative orthotopic tumor model due to its size, which is large enough to inject PMMA-Fe_3O_4 bone cement, and because the tibial plateau is a load-bearing bone; these characteristics can simulate bone tumor invasion in humans. This model can also provide sufficient sample to test both the efficacy of bone tumor ablation and the repair ability of these dual-function materials. The VX2 tumor is a virus-induced skin papilloma of rabbits that was first characterized in 1933 by Shope and Hurst [54], and the VX2 tumor model is considered the most suitable model for studying skeletal tumors [55, 56].

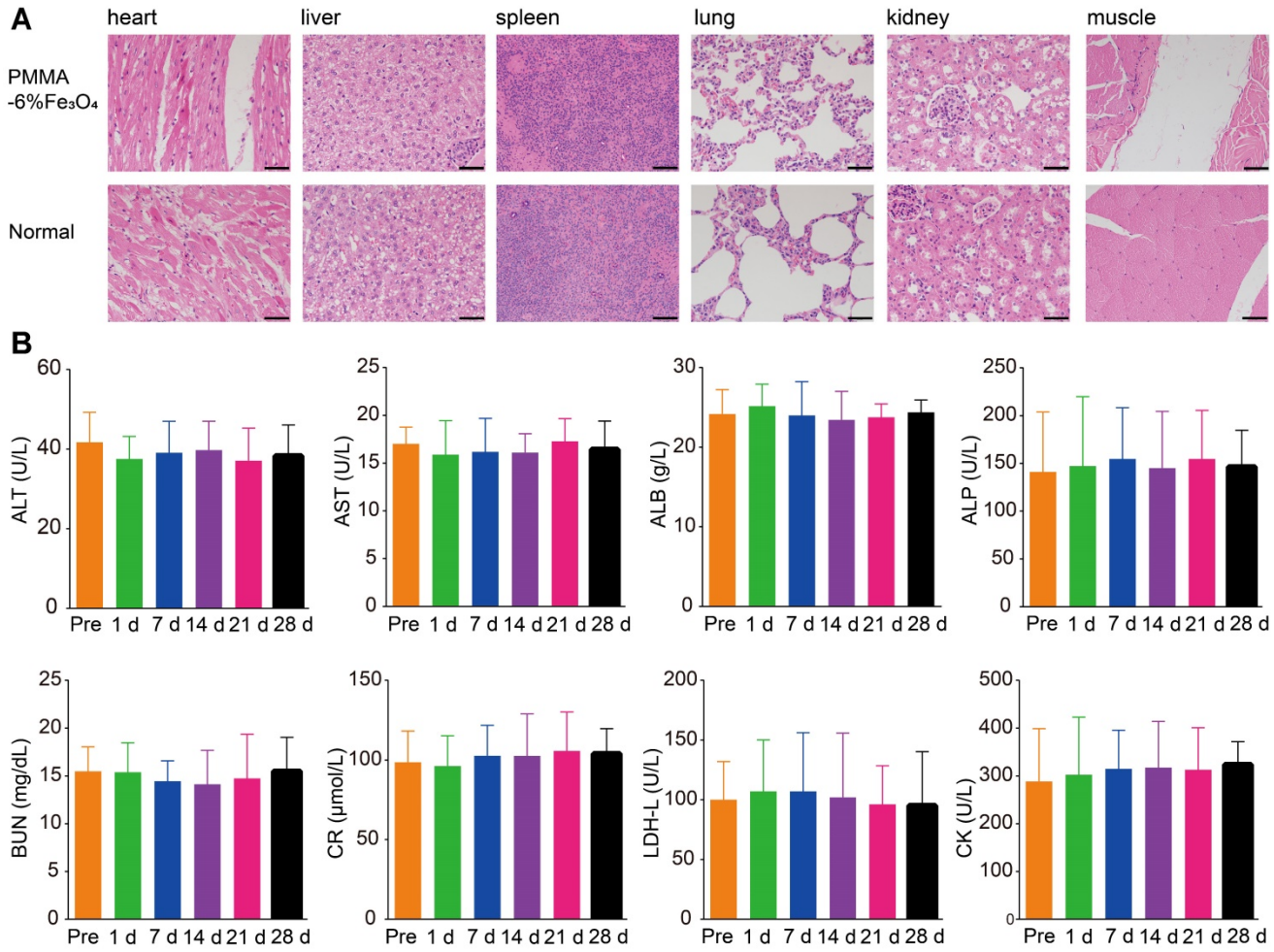

Figure 4. Biocompatibility and biosafety of PMMA-6%Fe_3O_4. (A) H&E staining of primary organs (heart, liver, spleen, lung, kidney) and muscle in healthy rabbits with and without injection of PMMA-6%Fe_3O_4 after 4 weeks. The scale bar is 50 μm. (B) Histograms depicting variations in serum biochemical parameters for alanine aminotransferase (ALT), aspartate aminotransferase (AST), creatinine (CR), blood urine nitrogen (BUN), creatine kinase (CK) and lactate dehydrogenase level (LDH-L) containing PMMA-6%Fe_3O_4 with different time points over 28 days.

Standard methods to establish a rabbit tibial plateau bone tumor with VX2 mass/cells involve cutting the skin to expose the bone surface, using a burr to drill a hole in the tibial plateau, placing a tumor mass in the hole, sealing the hole via bone wax and suturing the skin incision [57, 58]. These traditional procedures are complex, which may lower the efficiency of establishing the model. More importantly, in addition to the loss, the extensive trauma caused by drilling bone tissue will easily connect the drilled hole to the bone marrow cavity, which may change the model position and result in tumor metastasis, easily increasing the mortality [58, 59]. Therefore, it is critical to modify the methods to develop a novel model. In our method, the diameter of the puncture needle was only 1.2 mm **(Figure S8)**. With the guidance of the needle, the tumor mass could be accurately seeded in the tibial plateau, the operation procedures were extremely convenient and resulted in a small needle tract, and there was no incision to suture. After 13 to 15 days, the bone tumor reached a volume of 180.0 ± 15.0 mm^3 and was ideally located in the central cancellous bone of the tibial plateau, which was observed through CT and MRI examinations. Compared with subcutaneously implanted tumor models in mice, the in situ tibial plateau bone tumor model in rabbits better imitates the clinically common tibial plateau bone tumor. Taking advantage of this novel bone tumor model, we obtained a detailed understanding of the progression of bone tumors and demonstrated the exact treatment effect.

In vivo magnetic-thermal-induced ablation efficiency

After injection, the tumor was simply heated by putting the tumor-bearing rabbit leg in a water-cooled magnetic induction coil. Unlike the heating of subcutaneous tumor xenografts in nude mice [35, 51], the skin temperature increased slowly and gradually. Even after continuous heating for 150 s, the peak temperature was less than 55 °C **(Figure 5A and Figure 5C)**. This slow heating process indicated that the heating efficiency could be well controlled, thereby protecting healthy tissues. After heating, there was no obvious damage to the leg, such as skin shrinking, paleness, limb swelling or knee joint activity limitations; only slight transient hyperemia of the leg skin was found. Comparatively, there was no obvious temperature increase in the Tumor-H group after exposure to AMF for 150 s **(Figure 5A and Figure 5C)**.

The therapeutic effect was continuously and regularly examined via CT imaging. As **Figure 5B** shows, before injection, enhanced MRI images showed a low signal in the central tibial plateau with peripheral enhancement, and the corresponding coronal reconstructed CT images showed that the cancellous bone of the tibial plateau was destroyed by the tumor, leaving a cavity in the bone **(Figure S9E)** PMMA-6%Fe_3O_4 bone cement was easily be injected into the cavity with CT guidance due to its high fluidity. Postinjection CT images show that the PMMA-6%Fe_3O_4 bone cement distributed and filled the cavity well. This finding indicated that the PMMA-6%Fe_3O_4 bone cement was a highly injectable material and could be precisely injected *in vivo* under CT guidance. For the Tumor group, there was no obvious change in the CT images after injecting a saline solution.

During the follow-up, the rabbits in the PMMA-6%Fe_3O_4, Tumor and Tumor-H groups showed progressive knee joint swelling, fast growth of soft masses, progressive aggravation of knee joint activity limitations and severe body weight loss. Eventually, these rabbits were unable to stand properly and had to remain prostrate on the ground and depend only on the forelimb to move **(Figure S10)**. Unfortunately, these rabbits were too weak to survive for more than 1 month **(Figure 7D)** and died for visceral metastasis **(Figure S11)**. In comparison, most rabbits in the PMMA-6%Fe_3O_4-H group showed typical growth for 56 days, except three rabbits that did not survive the treatment duration **(Figure 7D)**. After dissection, two rabbits were found to have visceral metastasis, and the other one died from diarrhea. As shown in **Figure 5B and Figure 6A**, the volume of bone defects in the PMMA-6%Fe_3O_4-H group increased slightly at the 35-day follow-up. The absorbed bone tissue was located close to the bone marrow, likely caused by heating. The most exciting finding is that new bone formation was found after day 42; this new bone was located in the absorbed area. The CT value and thickness of the upper tibial plateau cortical bone obviously increased in the CT images, and compared to the preinjection measurements, the corresponding measurements on day 56 showed a significant increase **(Figure 5E-F)**. The new bone formation after tumor ablation confirms the excellent controllability of the heating area. PMMA-6%Fe_3O_4 with AMF can completely eliminate bone tumors without creating large lesions in the surrounding healthy tissues. The therapeutic process may result in minor injury of healthy bone structures, and these tissues can be regenerated with time. After injection of PMMA-Fe_3O_4, no tibial plateau fracture occurred in the PMMA-6%Fe_3O_4-H group, and the mobility was not compromised, which means that this dual-function material provides suitable mechanical properties.

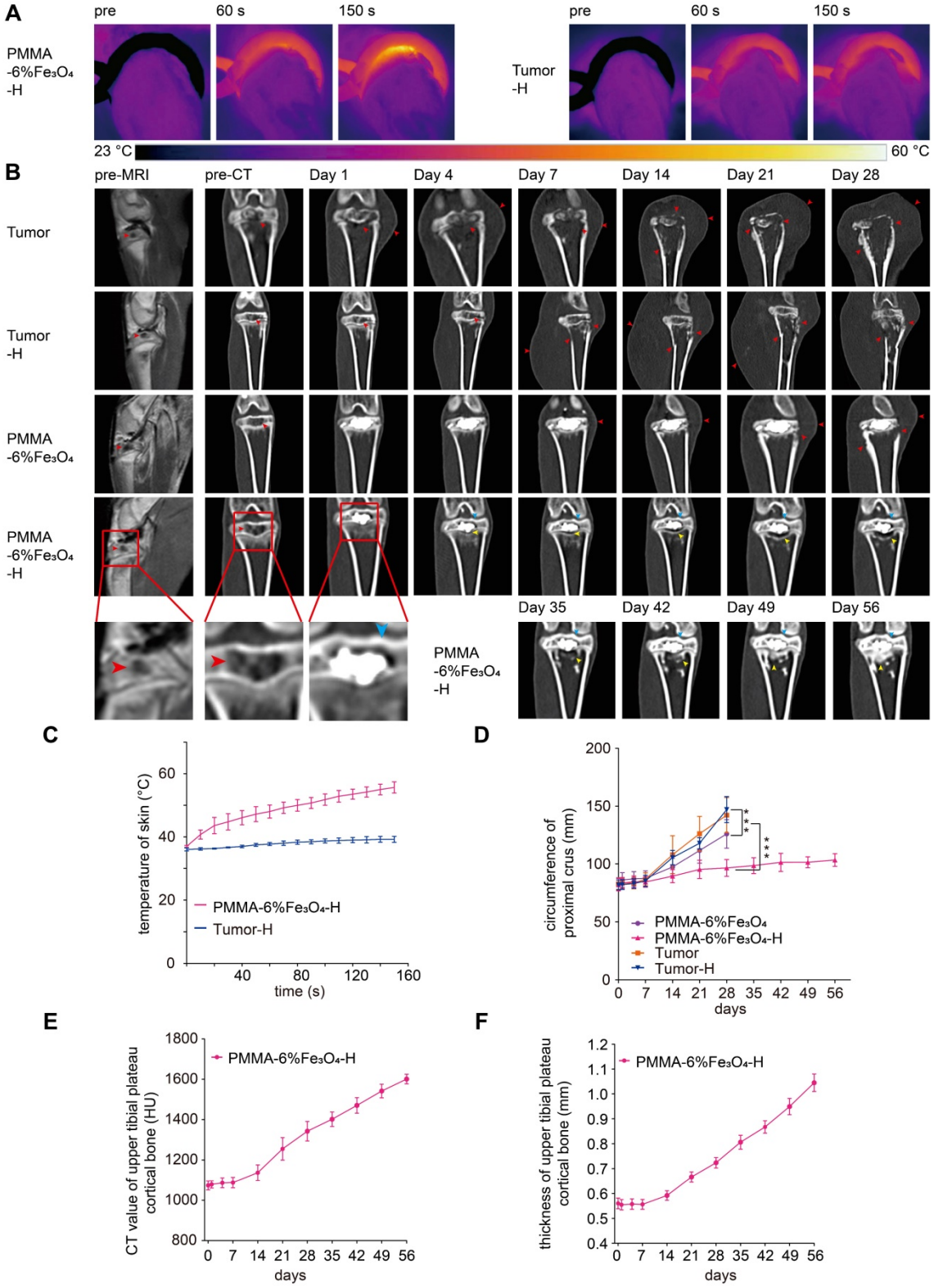

Figure 5. *In vivo* magnetic thermal therapy for tumor and follow-up CT coronal reconstruction examination. (A) Thermal images of rabbit leg in the PMMA-6%Fe_3O_4-H group and Tumor-H group and (C) the corresponding temperature-time curve. (B) Enhanced MRI images and coronal reconstructed CT images at each follow-up time point (red arrow: bone destruction and swelling of soft tissue, blue arrow: cortical bone of upper tibial plateau, yellow arrow: area of bone resorption and new bone formation). (D) Curve of the circumference of the proximal crus change over time. (E) Curve of the CT value of the upper tibial plateau cortical bone change over time. (F) Curve of the thickness of the upper tibial plateau cortical bone change over time.

In contrast, during the 28-day follow-up, the bone defect volume successively and significantly increased in the PMMA-6%Fe_3O_4, Tumor and Tumor-H groups, as indicated by the comparison between the preinjection and postinjection groups (175.7 ± 7.8 mm^3 vs. 412.1 ± 38.6 mm^3, 174.3 ± 6.6 mm^3

vs. 421.0 ± 30.0 mm^3 and 179.9 ± 5.9 mm^3 vs. 460.5 ± 28.5 mm^3, respectively, $p < 0.001$, **Figure 6B**). As the CT images show, both bone and soft tissues around the tibial plateau in the Tumor, Tumor-H and PMMA-6%Fe_3O_4 groups became obviously swollen with time, and the bone of the tibial plateau disappeared, demonstrating massive bone loss **(Figure 6A-B)**. The soft tissues around the tibial plateau also swelled severely in response to the tumor invasion **(Figure 5B)**, so the circumference of the proximal crus increased rapidly **(Figure 5D)**. At the 28-day of follow-up, the weight was significantly higher in the PMMA-6%Fe_3O_4-H group (2.4 ± 0.1 kg) than in the PMMA-6%Fe_3O_4, Tumor and Tumor-H groups (1.4 ± 0.3 kg, 1.7 ± 0.2 kg and 1.5 ± 0.1 kg, respectively, $p < 0.001$, **Figure 6C**). These results indicate that normal growth occurred in the PMMA-6%Fe_3O_4-H group, while the weight decreased in the control groups.

The microscopic therapeutic outcomes of tumor cells were evaluated by standard H&E staining. As **Figure 7A** shows, on day 1 after the intervention, a large area of uniformly red-stained cytoplasm, indicating disordered tissue and marked destruction of cells, was found in the PMMA-6%Fe_3O_4-H group. Comparatively, there was no obvious cell destruction in the control groups, which exhibited normal nuclei and cytoplasm. On day 4, the apoptosis and proliferation inhibition of the tumor cells in the PMMA-6%Fe_3O_4-H group increased, as indicated by TUNEL and PCNA assays, respectively. Comparatively, no obvious apoptosis or proliferation inhibition was observed in the Tumor and Tumor-H groups **(Figure 7B-C)**. In the PMMA-6%Fe_3O_4 group,

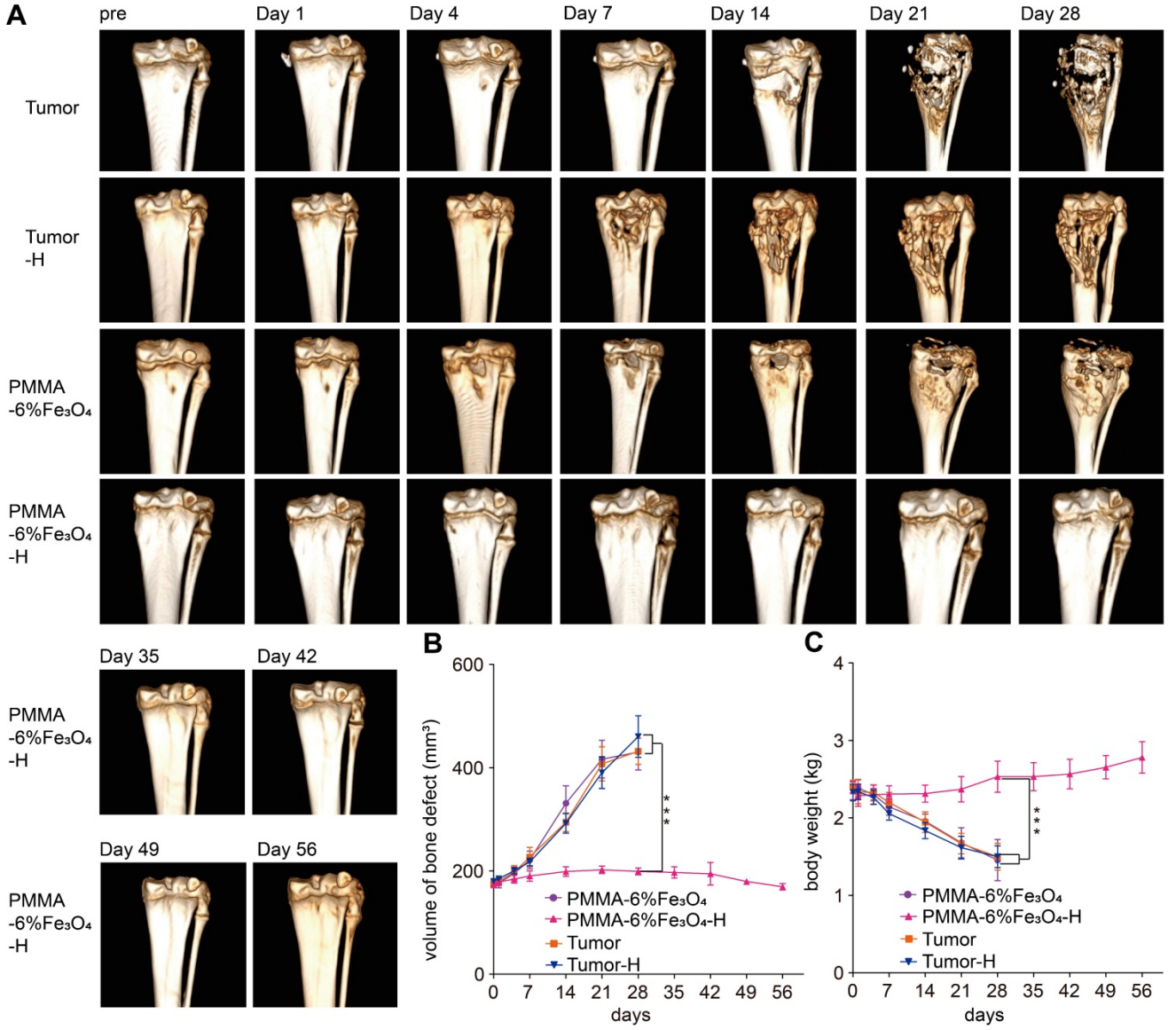

Figure 6. Follow-up CT 3D reconstruction examination. (A) 3D-reconstructed CT images at each follow-up time point. (B) Curve of the volume of bone defect change over time. (C) Curve of the body weight change over time.

there was no apoptosis, but slight proliferation inhibition was observed. This proliferation inhibition may result from the temporary high temperature during the polymerization of PMMA and a change in the internal microenvironment of the tumor after PMMA-Fe_3O_4 injection. Pathological analysis clearly demonstrated the therapeutic efficacy of PMMA-Fe_3O_4 implants exposed to an AMF. The morbidity-free survival curve is shown in **Figure 7D**. As shown in **Figure 7F**, the visceral metastasis percentages in the PMMA-6%Fe_3O_4-H, PMMA-6%Fe_3O_4, Tumor and Tumor-H groups were 14.3%, 71.4%, 57.1% and 64.3%, respectively. The corresponding visceral pathology indicated by H&E staining is shown in **Figure 7E**. Notably, two rabbits with visceral metastasis remained in the PMMA-6%Fe_3O_4-H group because the local tumors were ablated. The reason might be that visceral metastasis occurred before magnetic thermal ablation was applied. Like other types of thermal ablation, magnetic thermal ablation still has the shortcoming of incomplete ablation. For identified local tumors, magnetic thermal ablation exhibits high efficiency; however, for unknown metastatic tumors, another therapeutic modality needs to be explored in the future.

It has been reported that magnetic hyperthermia can induce the regression of distant metastatic tumors without heat when another local tumor is exposed to heat [60]. The HSPs presented in thermal-induced dying tumor cells are responsible for subsequent induction of antitumor immune responses [61]. The importance of HSPs, such as HSP-70, HSP-90 and gp96, in immune reactions has been demonstrated by several reports [62-64]. In this study, HSP-70 was detected 1 day after heating, and HSP-70 levels successively increased over the next 14 days in the heating group. The other two control groups showed no HSP-70 increase. Another significant cytokine is IL-2, which can reduce the immune response and inhibit the immune reaction of activated lymphocytes [65]. In this study, the expression of IL-2 in the PMMA-6%Fe_3O_4-H group decreased with time and eventually became lower than that in the groups without heating. Overall, the increase in HSP-70 and decrease in IL-2 indicate that hyperthermia can improve the host immune state and enhance antitumor treatments. In the PMMA-6%Fe_3O_4-H group, the level of HSP-70 successively increased, while the level of IL-2 successively decreased during the 14-day follow-up period. Comparatively, there were no obvious changes in the control groups **(Figure 7G-H)**. This result means hyperthermia therapy activated immunomodulation. However, this finding requires further experiments to evaluate the antitumor potential.

Conclusions

We have presented a highly efficient and minimally invasive approach for complete bone tumor regression and bone defect repair by magnetic thermal ablation based on PMMA containing Fe_3O_4 NPs; this approach shows excellent heating ability for rabbit VX2 tibial plateau tumor ablation upon exposure to an AMF and provides mechanical support for bone repair. The new and powerful dual-function implant is a promising minimally invasive agent for the treatment of bone tumors and has good clinical translation potential.

Abbreviations

NPs: nanoparticles; PMMA: polymethyl-methacrylate; SEM: scanning electron microscopy; Tmax: maximum temperature; Tset: setting time; CT: computed tomography; AMF: alternating magnetic field; PVP: percutaneous vertebroplasty; PKP: percutaneous kyphoplasty; CPC: calcium phosphate cement; MRI: magnetic resonance imaging; H&E: hematoxylin-eosin; HSPs: heat shock proteins; ICP-OES: inductively coupled plasma optical emission spectrometer; UVECs: umbilical vein endothelial cells; TUNEL: terminal deoxynucleotidyl transferase dUTP nick end labeling; PCNA: proliferating cell nuclear antigen; PI: proliferation index; AI: apoptotic index; IL-2: interleukin 2; WBC: white blood cell; RBC: red blood cell; HB: hemoglobin; PLT: platelet; ALT: alanine aminotransferase; AST: aspartate aminotransferase; CR: creatinine; BUN: blood urea nitrogen; CK: creatine kinase; LDH-L: lactate dehydrogenase levels.

Supplementary Material

Supplementary materials and methods, figures and table. http://www.thno.org/v09p4192s1.pdf

Acknowledgments

We acknowledge the financial support from the NSF for Distinguished Young Scholars (Grant No. 81425014), National Key R&D Program of China (2018YFC0115200), NSFC (Grant No. 81630047, No. 31630026 and No. 81672230), NSFC Key Projects of International Cooperation and Exchanges (81720108023) and Shanghai S&T Major Project (2018SHZDZX05). We acknowledge the Department of Radiology (Second Affiliated Hospital of Chongqing Medical University) for applying and directing MRI and CT.

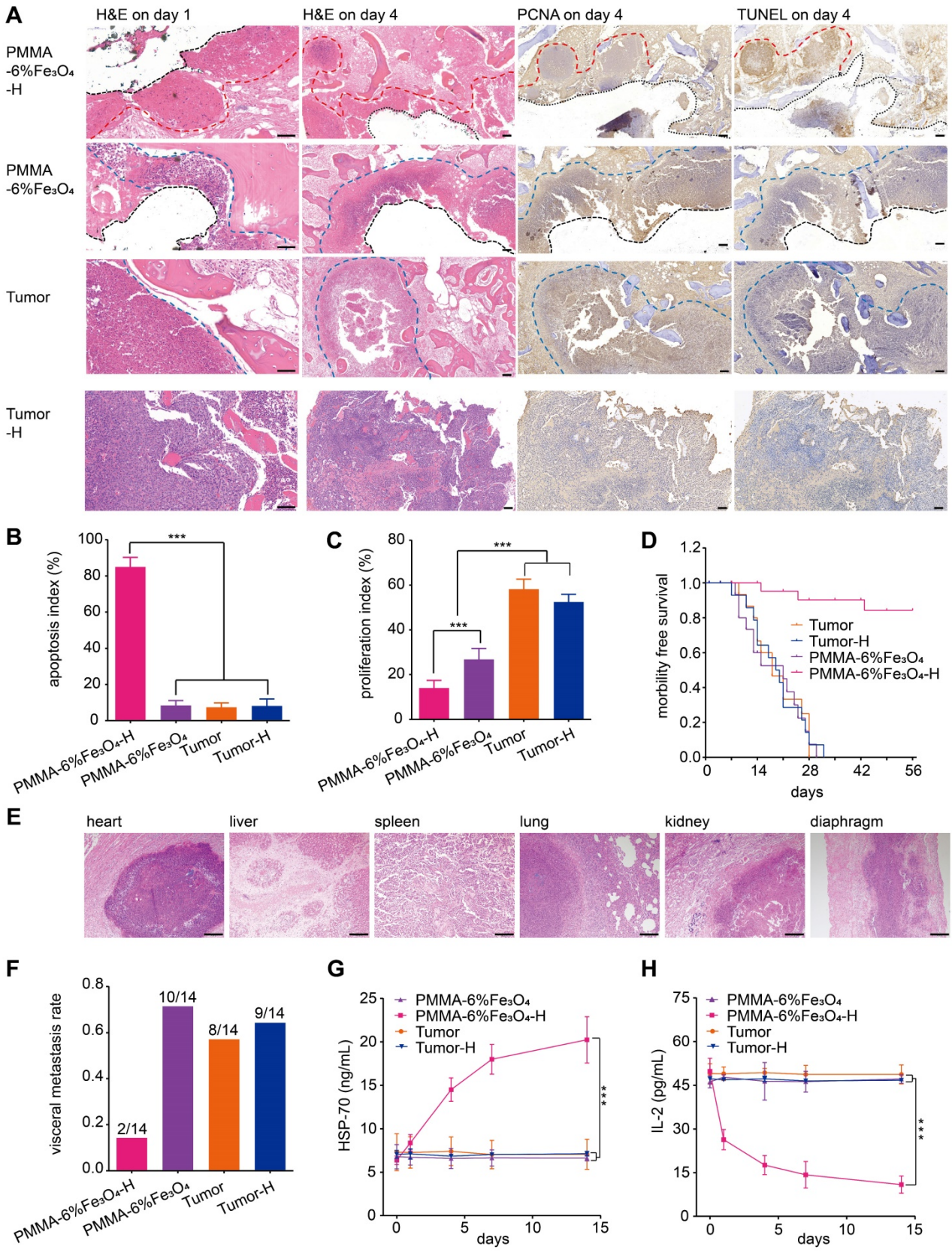

Figure 7. *In vivo* effects of PMMA-6%Fe_3O_4 on tumor suppression with magnetic thermal therapy. (A) H&E staining on day 1 (scale bar is 50 μm), and H&E staining, TUNEL assay and PCNA assay on day 4 (scale bar is 100 μm) (red dotted line: edge of ablation, blue dotted line: edge of the tumor, black dotted line: edge of removed PMMA-6%Fe_3O_4). (B) and (C) are the apoptosis index (AI) and the proliferation index (PI) of each group. (D) Morbility-free survival curves of tumor-bearing rabbits after different treatments. (E) H&E staining (scale bar is 200 μm) of metastasis organs (heart, liver, spleen, lung, kidney and diaphragm). (F) Visceral metastasis rate of tumor-bearing rabbits after different treatments. (G) HSP-70 levels of rabbit serum in different groups before and after magnetic thermal ablation. (H) IL-2 levels of rabbit serum in different groups before and after magnetic thermal ablation.

Author Contributions

KY, BL: planed, performed, analyzed experiments and wrote the manuscript. YZ: conceived the idea and designed the experiments. LC, ZD: planed and supervised experiments. AE, MK, TX: analyzed the data and wrote the manuscript. DG, XC, ZW, HR: primarily responsible for the data collection and analysis. All authors discussed the results and commented on the manuscript. Kexiao Yu and Bing Liang are co-first authors.

Competing Interests

The authors have declared that no competing interest exists.

References

1. Moore DD, Luu HH. Osteosarcoma. Cancer Treat Res. 2014; 162: 65-92.
2. Weilbaecher KN, Guise TA, McCauley LK. Cancer to bone: a fatal attraction. Nat Rev Cancer. 2011; 11: 411-25.
3. Schroeder A, Heller DA, Winslow MM, Dahlman JE, Pratt GW, Langer R, et al. Treating metastatic cancer with nanotechnology. Nat Rev Cancer. 2011; 12: 39-50.
4. Gartrell BA, Saad F. Managing bone metastases and reducing skeletal related events in prostate cancer. Nat Rev Clin Oncol. 2014; 11: 335-45.
5. Suva LJ, Griffin RJ, Makhoul I. Mechanisms of bone metastases of breast cancer. Endocr Relat Cancer. 2009; 16: 703-13.
6. Wang Y, Yang J, Liu H, Wang X, Zhou Z, Huang Q, et al. Osteotropic peptide-mediated bone targeting for photothermal treatment of bone tumors. Biomaterials. 2017; 114: 97-105.
7. Coleman RE. Clinical features of metastatic bone disease and risk of skeletal morbidity. Clin Cancer Res. 2006; 12: 6243-9.
8. Bhatt AD, Schuler JC, Boakye M, Woo SY. Current and emerging concepts in non-invasive and minimally invasive management of spine metastasis. Cancer Treat Rev. 2013; 39: 142-52.
9. Sosa MS, Bragado P, Aguirre-Ghiso JA. Mechanisms of disseminated cancer cell dormancy: an awakening field. Nat Rev Cancer. 2014; 14: 611-22.
10. Pantel K, Volkmar M, Auer M, Nusser N, Harbeck N, Braun S. Detection and clinical implications of early systemic tumor cell dissemination in breast cancer. Clin Cancer Res. 2003; 9: 6326-44.
11. Marlow R, Honeth G, Lombardi S, Cariati M, Hessey S, Pipili A, et al. A novel model of dormancy for bone metastatic breast cancer cells. Cancer Res. 2013; 73: 6886-99.
12. Huang H, Delikanli S, Zeng H, Ferkey DM, Pralle A. Remote control of ion channels and neurons through magnetic-field heating of nanoparticles. Nat Nanotechnol. 2010; 5: 602-6.
13. Lee JH, Jang JT, Choi JS, Moon SH, Noh SH, Kim JW, et al. Exchange-coupled magnetic nanoparticles for efficient heat induction. Nat Nanotechnol. 2011; 6: 418-22.
14. Johannsen M, Gneveckow U, Taymoorian K, Thiesen B, Waldofner N, Scholz R, et al. Morbidity and quality of life during thermotherapy using magnetic nanoparticles in locally recurrent prostate cancer: results of a prospective phase I trial. Int J Hyperthermia. 2007; 23: 315-23.
15. Wust P, Hildebrandt B, Sreenivasa G, Rau B, Gellermann J, Riess H, et al. Hyperthermia in combined treatment of cancer. Lancet Oncol. 2002; 3: 487-97.
16. Issels RD, Lindner LH, Verweij J, Wust P, Reichardt P, Schem BC, et al. Neo-adjuvant chemotherapy alone or with regional hyperthermia for localised high-risk soft-tissue sarcoma: a randomised phase 3 multicentre study. Lancet Oncol. 2010; 11: 561-70.
17. Zee JVD, González D, Rhoon GCV, Dijk JDV, Putten WLV, Hart AA. Comparison of radiotherapy alone with radiotherapy plus hyperthermia in locally advanced pelvic tumours: a prospective, randomised, multicentre trial. Lancet. 2000; 355: 1119-25.
18. Chen Y, Gao Y, Chen H, Zeng D, Li Y, Zheng Y, et al. Engineering inorganic nanoemulsions/nanoliposomes by fluoride-silica chemistry for efficient delivery/co-delivery of hydrophobic agents. Adv Funct Mater. 2012; 22: 1586-97.
19. Kennedy JE. High-intensity focused ultrasound in the treatment of solid tumours. Nat Rev Cancer. 2005; 5: 321-7.
20. Liu Y, Li T, Ma H, Zhai D, Deng C, Wang J, et al. 3D-printed scaffolds with bioactive elements-induced photothermal effect for bone tumor therapy. Acta Biomater. 2018; 73: 531-46.
21. Liu T, Wang C, Gu X, Gong H, Cheng L, Shi X, et al. Drug delivery with PEGylated MoS2 nano-sheets for combined photothermal and chemotherapy of cancer. Adv Mater. 2014; 26: 3433-40.
22. Thiesen B, Jordan A. Clinical applications of magnetic nanoparticles for hyperthermia. Int J Hyperthermia. 2008; 24: 467-74.
23. Derfus AM, von Maltzahn G, Harris TJ, Duza T, Vecchio KS, Ruoslahti E, et al. Remotely triggered release from magnetic nanoparticles. Adv Mater. 2007; 19: 3932-6.
24. Firanescu CE, de Vries J, Lodder P, Venmans A, Schoemaker MC, Smeet AJ, et al. Vertebroplasty versus sham procedure for painful acute osteoporotic vertebral compression fractures (VERTOS IV): randomised sham controlled clinical trial. BMJ. 2018; 361: 1551.
25. Lv Y, Li A, Zhou F, Pan X, Liang F, Qu X, et al. A novel composite PMMA-based bone cement with reduced potential for thermal necrosis. ACS Appl Mater Interfaces. 2015; 7: 11280-5.
26. Ormsby R, McNally T, O'Hare P, Burke G, Mitchell C, Dunne N. Fatigue and biocompatibility properties of a poly(methyl methacrylate) bone cement with multi-walled carbon nanotubes. Acta Biomater. 2012; 8: 1201-12.
27. Clark W, Bird P, Gonski P, Diamond TH, Smerdely P, McNeil HP, et al. Safety and efficacy of vertebroplasty for acute painful osteoporotic fractures (VAPOUR): a multicentre, randomised, double-blind, placebo-controlled trial. Lancet. 2016; 388: 1408-16.
28. Schroder C, Nguyen M, Kraxenberger M, Chevalier Y, Melcher C, Wegener B, et al. Modification of PMMA vertebroplasty cement for reduced stiffness by addition of normal saline: a material properties evaluation. Eur Spine J. 2017; 26: 3209-15.
29. Paz E, Forriol F, Real JCD, Dunne N. Graphene oxide versus graphene for optimisation of PMMA bone cement for orthopaedic applications. Mat Sci Eng C-Mater. 2017; 77: 1003.
30. Yuan Y, Ding Z, Qian J, Zhang J, Xu J, Dong X, et al. Casp3/7-instructed intracellular aggregation of Fe3O4 nanoparticles enhances T2 MR imaging of tumor apoptosis. Nano Lett. 2016; 16: 2686-91.
31. Kawashita M, Kawamura K, Li Z. PMMA-based bone cements containing magnetite particles for the hyperthermia of cancer. Acta Biomater. 2010; 6: 3187-92.
32. Xu C, Zheng Y, Gao W, Xu J, Zuo G, Chen Y, et al. Magnetic hyperthermia ablation of tumors using injectable Fe(3)O(4)/calcium phosphate cement. ACS Appl Mater Interfaces. 2015; 7: 13866-75.
33. Burguera EF , Xu HHK , Sun L. Injectable calcium phosphate cement effects of powder-to liquid ratio and needle size. J Biomed Mater Res B Appl Biomater. 2008; 84: 493-502.
34. Nedkov I, Slavov L, Merodiiska T, Lukanov P, Tailhades PH, Gougeon M, et al. Size effects in monodomain magnetite based ferrofluids. J Nanopart Res. 2008; 10: 877-880.
35. Ling Y, Tang X, Wang F, Zhou X, Wang R, Deng L, et al. Highly efficient magnetic hyperthermia ablation of tumors using injectable polymethylmethacrylate–Fe3O4. RSC Adv. 2017; 7: 2913-8.
36. Birkenmaier C, Baumert S, Schroeder C, Jansson V, Wegener B. A biomechanical evaluation of the epidural neurolysis procedure. Pain Physician. 2012; 15: 89-97.
37. Hai-long R, Jian-ming J, Jian-ting C, Ji-xing W. Risk factors of new symptomatic vertebral compression fractures in osteoporotic patients undergone percutaneous vertebroplasty. Eur Spine J. 2015; 24: 750-8.
38. Rho YJ, Choe WJ. Risk factors predicting the new symptomatic vertebral compression fractures after percutaneous vertebroplasty or kyphoplasty. Eur Spine J. 2012; 21: 905-11.
39. Mudano AS, Bian J, Cope JU, Curtis JR, Gross TP, Allison JJ, et al. Vertebroplasty and kyphoplasty are associated with an increased risk of secondary vertebral compression fractures: a population-based cohort study. Osteoporosis Int. 2009; 20: 819-26.
40. Kolb JP, Kueny RA. Pu¨schel K, Boger A, Rueger JM, Morlock MM, et al. Does the cement stiffness affect fatigue fracture strength of vertebrae;after cement augmentation in osteoporotic patients? Eur Spine J. 2013; 22: 1650-6.
41. López A, Mestres G, Ott MK, Engqvist H, Ferguson SJ, Persson C, et al. Compressive mechanical properties and cytocompatibility of bone-compliant, linoleic acid-modified bone cement in a bovine model. J Mech Behav Biomed Mater. 2014; 32: 245-56.
42. Ahn DK, Lee S, Choi DJ, Park SY, Woo DG, Kim CH, et al. Mechanical properties of blood-mixed polymethylmetacrylate in percutaneous vertebroplasty. Asian Spine J. 2009; 3: 45-52.
43. Landers J, Salamon S, Remmer H, Ludwig F, Wende H. Simultaneous study of brownian and neel relaxation phenomena in ferrofluids by mossbauer spectroscopy. Nano lett. 2016; 16: 1150-5.
44. Mamiya H, Jeyadevan B. Design criteria of thermal seeds for magnetic fluid hyperthermia – from magnetic physics point of view. In: Fratila R, Ed. Nanomaterials for magnetic and optical hyperthermia applications, 1st ed. Amsterdam, Netherlands: Elsevier Publisher; 2019: 13-39.
45. Tay ZW, Chandrasekharan P, Chiu-Lam A, Hensley DW, Dhavalikar R, Zhou XY, et al. Magnetic particle imaging guided heating in vivo using gradient fields for arbitrary localization of magnetic hyperthermia therapy. Acs Nano. 2018; 12: 3699-3713.
46. Liu JF, Neel N, Dang P, Lamb M, Mckenna J, Rodgers L, et al. Radiofrequency-triggered drug release from nanoliposomes with millimeter-scale resolution using a superimposed static gating field. Small. 2018;14: e1802563.
47. Mohamed M, Borchard G, Jordan O. In situ forming implants for local chemotherapy and hyperthermia of bone tumors. J Drug Deliv Sci Technol. 2012; 22: 393-408.

48. Hilger I, Hiergeist R, Hergt R, Winneffld K, Schubert H, Kaiser WA. Thermal ablation of tumors using magnetic nanoparticles: an in vivo feasibility study. Invest Radiol. 2002, 37: 580-586.
49. Liapi E, Geschwind JF. Transcatheter and ablative therapeutic approaches for solid malignancies. J Clin Oncol. 2007; 25: 978-86.
50. Chu KF, Dupuy DE. Thermal ablation of tumours: biological mechanisms and advances in therapy. Nat Rev Cancer. 2014; 14: 199-208.
51. Chen Y, Jiang L, Wang R, Lu M, Zhang Q, Zhou Y, et al. Injectable smart phase-transformation implants for highly efficient in vivo magnetic-hyperthermia regression of tumors. Adv Mater. 2014; 26: 7468-73.
52. Gao W, Zheng Y, Wang R, Chen H, Cai X, Lu G, et al. A smart, phase transitional and injectable DOX/PLGA-Fe implant for magnetic-hyperthermia-induced synergistic tumor eradication. Acta Biomater. 2016; 29: 298-306.
53. Makhoul I, Montgomery CO, Gaddy D, Suva LJ. The best of both worlds - managing the cancer, saving the bone. Nat Rev Endocrinol. 2016; 12: 29-42.
54. Shope RE, Hurst EW. Infectious papillomatosis of rabbits. J Exp Med. 1933; 58: 607-24.
55. Galasko CS. Mechanisms of lytic and blastic metastatic disease of bone. Clin Orthop Rel Res. 1982; 169: 20.
56. Wang HM, Crank S, Oliver G, Galasko CS. The effect of methotrexate-loaded bone cement on local destruction by the VX2 tumour. J Bone Joint Surg Br. 1996; 78: 14.
57. Choi JA, Kang EY, Kim HK, Song IC, Kim YI, Kang HS. Evolution of VX2 carcinoma in rabbit tibia: magnetic resonance imaging with pathologic correlation. Clin Imaging. 2008; 32: 128-35.
58. Wu R, Hu B, Kuang SL, Jiang LX, Huang Y, Ma F, et al. A rabbit bone tumor model for high-intensity focused ultrasound therapy. Minim Invasive Ther Allied Technol. 2011; 20: 206-11.
59. Suva LJ, Washam C, Nicholas RW, Griffin RJ. Bone metastasis: mechanisms and therapeutic opportunities. Nat Rev Endocrinol. 2011; 7: 208-18.
60. Yanase M, Shinkai M, Honda H, Wakabayashi T, Yoshida J, Kobayashi T. Antitumor immunity induction by intracellular hyperthermia using magnetite cationic liposomes. Jpn J Cancer Res. 1998; 89: 775-82.
61. Takeshi K, Kazuhiro K, Eiichi N, Kowichi J. Antitumor immunity by magnetic nanoparticle-mediated hyperthermia. Nanomedicine. 2014; 9: 1715-26.
62. Basu S, Binder RJ, Suto R, Anderson KM, Srivastava PK. Necrotic but not apoptotic cell death releases heat shock proteins, which deliver a partial maturation signal to dendritic cells and activate the NF-kappa B pathway. Int Immunol. 2000; 12: 1539.
63. Srivastava PK, Udono H, Blachere NE, Li Z. Heat shock proteins transfer peptides during antigen processing and CTL priming. Immunogenetics. 1994; 39: 93-8.
64. Udono H, Srivastava PK. Heat shock protein 70-associated peptides elicit specific cancer immunity. J Exp Med. 1993; 178: 1391-6.
65. Yang Y, Wang F, Zheng K, Deng L, Yang L, Zhang N, et al. Injectable PLGA/Fe3O4 implants carrying cisplatin for synergistic magnetic hyperthermal ablation of rabbit VX2 tumor. PLoS One. 2017; 12: e0177049.